

# Time-Dependent Hartree-Fock Approach to Nuclear Pasta at Finite Temperature

B. Schuetrumpf<sup>1</sup>, M. A. Klatt<sup>2</sup>, K. Iida<sup>3</sup>, J. A. Maruhn<sup>1</sup>, K. Mecke<sup>2</sup>, P.-G. Reinhard<sup>2</sup>

<sup>1</sup>*Institut fuer Theoretische Physik, Universitaet Frankfurt, D-60438 Frankfurt, Germany*

<sup>2</sup>*Institut fuer Theoretische Physik, Universitaet Erlangen-Nuernberg, D-91058 Erlangen, Germany and*

<sup>3</sup>*Department of Natural Science, Kochi University, 2-5-1 Akebono-cho, Kochi 780-8520, Japan*

(Dated: July 18, 2018)

We present simulations of neutron-rich matter at subnuclear densities, like supernova matter, with the time-dependent Hartree-Fock approximation at temperatures of several MeV. The initial state consists of  $\alpha$  particles randomly distributed in space that have a Maxwell-Boltzmann distribution in momentum space. Adding a neutron background initialized with Fermi distributed plane waves the calculations reflect a reasonable approximation of astrophysical matter. This matter evolves into spherical, rod-like, and slab-like shapes and mixtures thereof. The simulations employ a full Skyrme interaction in a periodic three-dimensional grid. By an improved morphological analysis based on Minkowski functionals, all eight pasta shapes can be uniquely identified by the sign of only two valuations, namely the Euler characteristic and the integral mean curvature.

PACS numbers: 26.50.+x, 21.60.Jz, 21.65.-f, 97.60.BW

## I. INTRODUCTION

Core-collapse supernovae (see, [1, 2] for a review) are considered to be relevant for many astrophysical phenomena including synthesis of heavy nuclei, acceleration of cosmic rays, and formation of neutron stars and black holes. The mechanism of such supernovae, however, has yet to be clarified, although hydrodynamics simulation studies of stellar collapse and subsequent explosion continue to be improved with respect to dimensionality and neutrino transport as well as inclusion of general relativity, rotation, and magnetic fields [3]. For such clarification, the properties of matter that constitutes the supernova cores such as the equation of state, the nuclei present, and the neutrino opacity are indispensable. This matter, which is believed to be charge-neutral and mostly beta-equilibrated while having a degenerate gas of electron neutrinos trapped inside, is often referred to as supernova matter. In early studies of supernova matter below normal nuclear density and at temperatures of order or lower than 10 MeV, nuclei in equilibrium were shown to be relatively neutron-rich by using a liquid-drop model [4], a Thomas-Fermi theory [5], and a Hartree-Fock (HF) theory [6].

At densities just below normal nuclear density, nearly spherical nuclei arranged in a Coulomb lattice and embedded in a roughly uniform neutralizing background of electrons are so closely packed that the total surface area becomes very large. Then, the system tends to lower the total surface area by elongating the nuclei and forming nuclear rods [7, 8]. It was predicted from seminal liquid-drop calculations [9, 10] that with further increase in density, the shapes of inhomogeneous nuclear matter change from rods to slabs, tubes, and bubbles until the system melts into uniform matter. These exotic nuclear configurations are often denoted as pasta nuclei, which arise from subtle competition between the surface and Coulomb energies. The pasta nuclei are manifestations of liquid-gas mixed phases of nuclear matter, among which

the phases with rods, slabs, and tubes can be regarded as liquid crystals [11].

In the conventional liquid-drop approach [9, 12], pasta nuclei were studied by assuming a geometrical shape of nuclear matter and using the Wigner-Seitz approximation. For more realistic description of pasta nuclei, multi-dimensional calculations without any assumption of the geometrical shape were performed in the Thomas-Fermi approach [13, 14], the Hartree-Fock approach [15], and the quantum molecular dynamics (QMD) approach [16, 17]. In these calculations, the shapes assumed in the Wigner-Seitz approximation were reproduced, while some cases did indicate the presence of more complex structures.

Astrophysically, the possible influence of pasta nuclei on the neutrino opacity may affect supernova explosions and subsequent proton-neutron star cooling. The cross section for the neutrino-nucleus scattering depends on the structure of inhomogeneous nuclear matter [18–20]. In fact, the neutrino scattering processes are no longer coherent in the directions in which nonspherical nuclei are elongated. This is a great contrast to the case of roughly spherical nuclei of which the finiteness in any direction leads to constructive interference in the scattering.

Recently, a time-dependent Hartree-Fock (TDHF) approach has been utilized to describe pasta nuclei in zero-temperature supernova matter [21, 22]. In contrast to static calculations which concentrate on the one configuration at minimal energy, the TDHF approach allows nucleons to explore multiple low-lying configurations in the energy landscape mapped by the time evolution of the mean field. In this work we perform such dynamic calculations at finite temperature, which are expected to give a realistic description of supernova matter as long as two-nucleon collisions can be ignored. As we shall see, the resultant map of pasta shapes is basically consistent with the phase diagrams obtained from the QMD calculations [17].

The TDHF simulations produce a great variety of very

involved, three dimensional structures. One needs tools to characterize a given configuration in terms of a few key numbers. This is simple for single finite nuclei where radius and a couple of deformation parameters serve very well. However, we encounter here compounds where much less is known ahead of time. For example, we do not even know the number of subunits or their connectivity. A very general and powerful means to quantify complex structures is provided by the Minkowski functionals, shape descriptors from integral geometry [23, 24]. These measures of structure are important tools in statistical physics [25–27] and pattern analysis [28, 29]. They were already introduced to astronomy for structure analysis of galaxy clusters in Ref. [30] and later used to investigate both point processes in cosmology [31, 32] and the cosmic microwave background [33]. Such Minkowski functionals provide, of course, the optimal technique to quantify pasta matter and so classify the different possible shapes. This had already been exploited in [34–36]. We aim to continue and deepen studies along this line.

In Sec. II, the TDHF approach is briefly reviewed. In Sec. III, a finite-temperature map of pasta shapes for inhomogeneous nuclear matter is presented. With the help of Minkowski functionals given in Sec. IV, we do morphological identifications of various phases in the map of pasta shapes in Sec. V. In Sec. VI we investigate thermal fluctuations in the density profiles and discuss their connection with melting of the inhomogeneous structures. Concluding remarks are given in Sec. VII.

## II. TDHF DESCRIPTION

In this framework, we want to describe the pasta structure with the time-dependent Hartree-Fock (TDHF) approximation. TDHF is a self-consistent mean field theory which was originally proposed by Dirac in 1930 [37]. In general, the TDHF equations are derived from a time-dependent variational principle with the variational space restricted to one single, time dependent Slater determinant. In nuclear applications, TDHF usually employs an effective interaction as, e.g., the Skyrme force, for a review see [38]. The treatment becomes then practically identical to a time-dependent density functional theory in local density approximation as it is widely used in electronic systems, see e.g. [39]. Computational limitations restricted earlier TDHF calculations in system size or symmetry [40, 41]. With the advance of computational power, it is now possible to perform full 3D calculations without any symmetry restrictions even for a large number of wave functions. This led to a revival of nuclear TDHF studies in various dynamical regimes as, e.g., collective vibrations [42, 43], large amplitude motion in fusion and nuclear reactions [44, 45], or, similar as done here, for simulations of stellar matter [21, 22].

The TDHF calculations are performed on an equidistant 3D grid in coordinate space with 16 grid points in each direction with a grid spacing of 1 fm. As usually

done in the physics of extended systems, we simulate infinite matter in a finite box with periodic boundary conditions. The Coulomb problem is solved with assumed global neutrality which means that we compensate the proton charges by a homogeneous negatively charged background which is supposed to simulate the electron gas around. This amounts to use the Coulomb solver with periodic boundary conditions and skipping the zero momentum component of the Coulomb field in Fourier space. The kinetic energy operator is evaluated in Fourier space and time evolution is performed using a Taylor expansion of the mean-field propagator. For the present calculations we choose Skyrme parametrization SLy6 which was developed with an emphasis on describing neutron rich matter [46].

## III. MAP OF REGIMES

### A. Initialization

We consider matter with a proton fraction of  $X_p = 1/3$ . In order to produce not too high excitations, we initialize the calculations by distributing a number  $N_\alpha$  of  $\alpha$  particles randomly over the grid keeping a minimal distance between each  $\alpha$  core to avoid perturbations by the overlap. To that end, we use ground wavefunctions for the  $\alpha$  particles produced before in a stationary HF calculation. The number  $N_\alpha$  is varied to produce systems with different densities. These  $\alpha$  cores are distributed in momentum space following a Maxwell-Boltzmann distribution with a given initialization temperature  $T_{\text{init}}$ . Further neutron states are introduced as plane wave states using a Fermi distribution with the same temperature to describe free background neutrons. Note that always both spin up and spin down states are occupied simultaneously to avoid a large spin excitation. Finally, before starting the TDHF calculation, these wave functions have to be ortho-normalized.

This randomized setup leads usually to a system without any symmetry. The time evolution is assumed to be sufficiently chaotic such that robust final states properties are reached which depend only on temperature and average density, although there are some regions where two states compete and the final outcome depends also on the initialization. The average density is tuned by the number of particles and the temperature by  $T_{\text{init}}$  in the sampling of  $\alpha$  particles and neutrons. Even with  $T_{\text{init}} = 0$  we store a considerable amount of excitation in the system stemming from the interaction energy of the  $\alpha$  particles.

### B. Temperature

The excitation state of matter is characterized by its actual temperature  $T$ . It is, however, difficult to measure temperature in the quantum simulation of a micro-

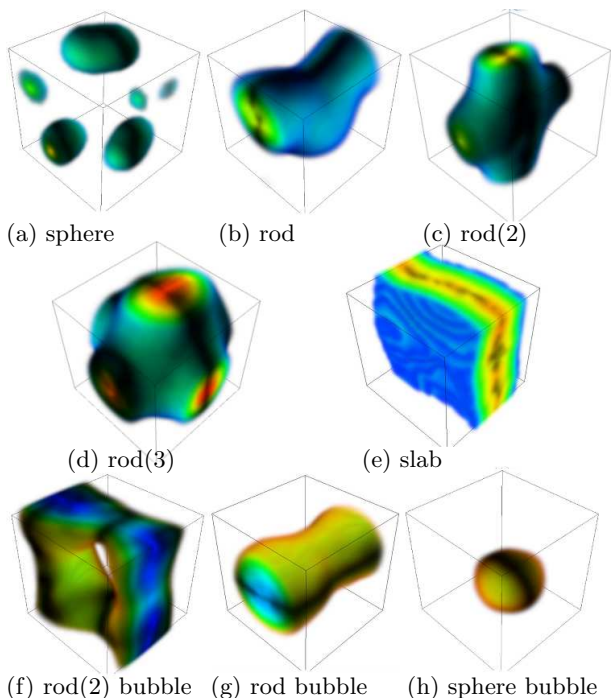


FIG. 1. Typical shapes of pasta structures at the lowest temperatures. These continue to evolve with time but do not change their morphological character anymore. Bubble shape illustrations show gas phase, which is indicated by the color-scale.

canonical ensemble as generated by the present TDHF calculations. As a rough measure, we estimate  $T$  by the excitation energy  $E^*$  through the relation  $E^* = (\pi^2 A)(2\varepsilon_F)T^2$  where  $A$  is the total number of nucleons and  $\varepsilon_F$  the Fermi energy of the system [47]. The excitation energy  $E^*$  is defined as the difference of the actual energy  $E$  to the ground state energy  $E_0$ . The latter is computed by solving the static HF problem for the given density. This amounts to

$$T = \frac{1}{\pi} \sqrt{2\varepsilon_F \frac{E^*}{N}}. \quad (1)$$

This excitation temperature  $T$  is to be distinguished from the “initial temperature”  $T_{\text{init}}$  which we use to boost stochastically the initial ensemble of  $\alpha$  particles and the background neutrons. Calculating the excitation temperature  $T$  for the different values of the initial temperature  $T_{\text{init}}$ , we find empirically  $T \approx 7 \text{ MeV} + \sqrt{T_{\text{init}}(T_{\text{init}} + 100 \text{ MeV})}/6$ . This is taken henceforth for a rough calibration of  $T$ .

### C. First overview

Each setup is evolved in time for 1500 fm/c. After that time, shapes do not change significantly. The system goes over into a pasta state where some type of equilibrium is achieved. Depending on the temperature differently

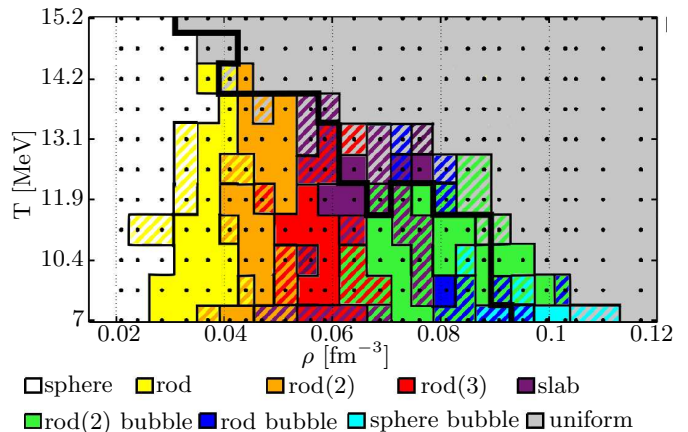


FIG. 2. Map of pasta shapes achieved in a TDHF calculation starting from a gas of  $\alpha$  particles with neutron background for various real temperatures and mean densities. The proton fraction is 1/3. Each dot represents two calculations. The solid black line shows a phase separation line discussed in Sec. VI.

strong fluctuations can be observed.

In FIG. 1 many different pasta shapes are classified. Among the structures found are rod and slab structures which have been discovered, e.g., by QMD calculations [36]. Rod(2) corresponds to rods forming a two-dimensional layer. The shape rod(3) describes three rods in x-, y- and z-direction which cross in one point. Similar shapes were discovered in [21, 48] and the rod(3) structure was also found in [15].

FIG. 2 shows for which density and temperature the different shapes appear. Note that two calculations for each point in the map were performed. As we have random initial conditions, the final shapes may differ although the same values for temperature and mean density are assumed. The hatched areas with a mixture of colors indicate the different final states reached in these cases. At higher densities, bubble structures can be seen (the gas phase has a pasta like shape). Many shapes can coexist here in one point of the map.

In the region of slab and rod(3) structures, the final state which is formed seems to highly depend on the initial condition. The similarity of these two structures is, that the liquid phase and gas phase have the same shapes. So gas and liquid phase symmetrically complement each other and fill out almost the same volume.

## IV. MINKOWSKI FUNCTIONALS

As already outlined in section I, a powerful tool to quantify the involved pasta shapes are Minkowski functionals [26]. There are four Minkowski functionals  $W_\nu$  defined for a spatial domain  $K$  in three dimensions: they are proportional to its volume  $W_0 \propto V$ , its surface-area  $W_1 \propto A$ , the integral mean curvature  $W_2 \propto \int_{\partial K} dA (\kappa_1 +$

TABLE I. Minkowski functionals in three dimensions evaluated for a domain  $K$ , with  $\kappa_1$  and  $\kappa_2$  the principle curvatures on  $\partial K$ .

$W_0$	$\propto$	$V$	volume
$W_1$	$\propto$	$\int_{\partial K} dA$	surface
$W_2$	$\propto$	$\int_{\partial K} dA (\kappa_1 + \kappa_2)/2$	int. mean curvature
$W_3$	$\propto$	$\int_{\partial K} dA \kappa_1 \cdot \kappa_2$	Euler characteristic

$\kappa_2)/2$ , and the topological Euler-Poincaré characteristic  $W_3 \propto \chi$ , which is equal to the integrated Gaussian curvature  $\int_{\partial K} dA \kappa_1 \cdot \kappa_2$ . Here,  $\kappa_1$  and  $\kappa_2$  are the principle curvatures on  $\partial K$ , the bounding surface of  $K$ . The Euler characteristic is a topological constant. TAB. I summarizes these definitions of the Minkowski functionals.

Minkowski functionals are useful shape descriptors. They are robust against noise and have short computation times, both due to their additivity property. These shape indices form a complete basis of all functionals defined on unions of convex sets which are translational and rotational invariant, additive, and at least continuous on convex sets [49]. Thus, the Minkowski functionals provide a complete scalar morphological characterization of the pasta shapes these functionals. The Minkowski functionals can be generalized to Minkowski tensors for an anisotropic structure characterization [27].

The TDHF results for pasta matter are given as grayscale data with a density  $\rho_i$  assigned to each voxel  $i$  (= grid point). In order to compute the Minkowski functionals of a domain  $K$ , the density field is turned into binary data via thresholding. A threshold density  $\rho_{th}$  is introduced. Each voxel  $i$  with  $\rho_i \geq \rho_{th}$  is set to black, but if  $\rho_i < \rho_{th}$ , white is assigned. The Minkowski functionals of the union of all black voxels, interpreted as a polygon  $K$ , can quantify the shape of the pasta matter in dependence of  $\rho_{th}$ . Beforehand however, the marching cube algorithm [28] is applied, which provides a smoothed polygonal representation in order to reduce voxelization errors. The Minkowski functionals of the polygon are evaluated, e.g., using the linear-time algorithm from Refs. [27, 50] [51].

The threshold density can take on values  $\rho_{th} \in [0, \rho_{max}]$ . But for small thresholds  $\rho_{th} \approx 0$  and for high thresholds  $\rho_{th} \approx \rho_{max}$ , the Minkowski functionals show erratic behavior; thus, the structure values for these thresholds are ignored [27, 52].

## V. STRUCTURE CLASSIFICATION

Calculating the values of the Minkowski scalars for all shapes as a function of threshold density (FIG. 3), we see that we can uniquely classify the different shapes in simple fashion: only the signs of integral mean curvature and Euler characteristic are needed (see TAB. II).

The central regime with solid lines in FIG. 3 indi-

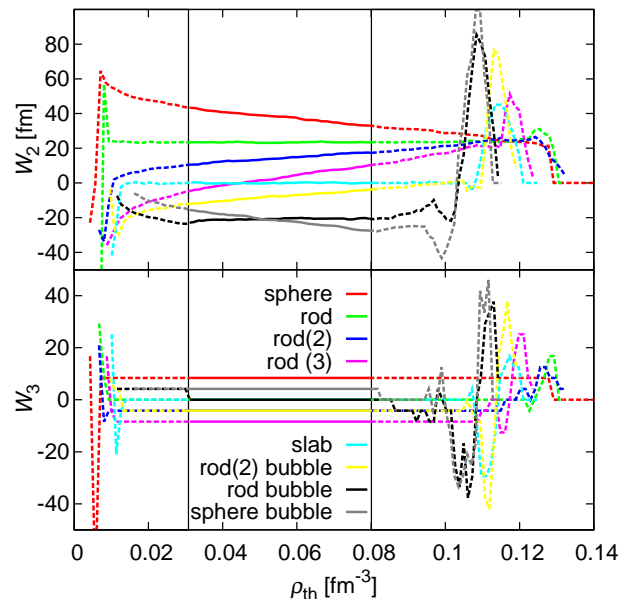


FIG. 3.  $W_2$ , proportional to the integral mean curvature, and  $W_3$ , proportional to the Euler characteristic as function of threshold density for the samples shown in FIG.1.

cate the physical values for the threshold density which yield reliably stable values of  $W_2$  and  $W_3$  for pasta configurations with the lowest value of temperature are  $\rho_{th} \in [0.03 \text{ fm}^{-3}, 0.08 \text{ fm}^{-3}]$ . For lower threshold densities only few dots are recognized as “white” (below threshold density) due to quantum fluctuations in the gas phase. At higher densities quantum fluctuations of the liquid phase are observed.

Rod(2), rod(2) bubble, and rod(3) consist in channels and tunnels; thus, the domain has a negative Euler characteristic  $\chi < 0$  [53].

The bubble shapes are the complements of the according sphere, rod, or rod(2) shapes. As the sign of both main curvatures  $\kappa_1$  and  $\kappa_2$  changes, the mean curvature  $H = (\kappa_1 + \kappa_2)/2$  also changes sign and so does  $W_2$ . However, the Gaussian curvature  $G = \kappa_1 \cdot \kappa_2$  and thus the Euler characteristic remain constant.

Both the slab and the rod(3) shape are symmetric in gas and liquid phase, as described in Sec. III. The shape of the liquid phase at low thresholds corresponds to the gas phase at high thresholds. Thus, the integral mean curvature as a function of the threshold  $\rho_{th}$  is point symmetric w.r.t. a mid value for the threshold density. This

TABLE II. Signs of the integral mean curvature and Euler characteristic for each observed shape.

shape	sph	rod	rod(2)	rod(3)	slab	rod(2) b	rod b	sph b
$W_2 > 0$	> 0	> 0	> 0	- to +	$\approx 0$	< 0	< 0	< 0
$W_3$	> 0	= 0	< 0	< 0	= 0	< 0	= 0	> 0



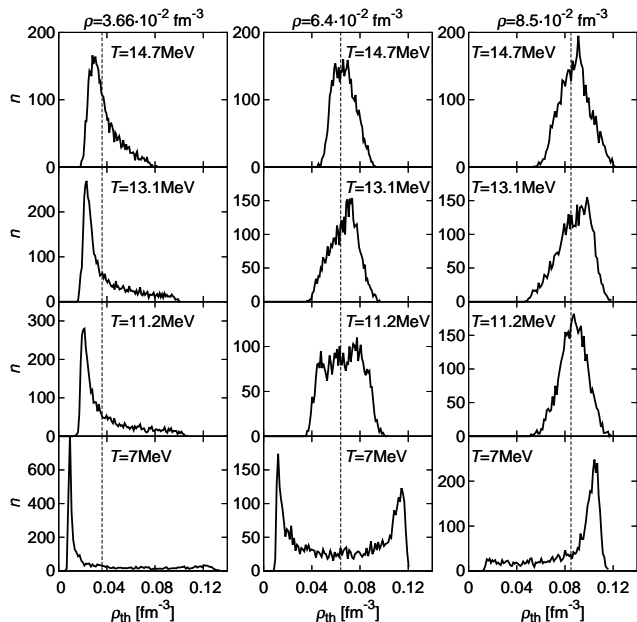


FIG. 4. Threshold density profiles for calculations varying in density and temperature. On each single plot the number of grid points  $n$  corresponding to a certain density value is plotted. The dashed lines show the mean density.

is trivially true for the slab with  $W_2 \approx 0$ , but holds also for the non-zero mean curvature of rod(3).

The results indicate that for a complete classification of the observed pasta shapes, the integral mean curvature as a function of  $\rho_{th}$  must be known.

Especially at higher temperatures and mean densities mixtures of phases can appear, in a sense that at different threshold densities the pasta matter can take on different shapes (cf. [22]). With increasing threshold densities the shapes can change to shapes which appear usually at lower mean densities e.g. a rod(2) bubble shape can take on a slab shape at higher values of  $\rho_{th}$ . For these cases we take the pasta phase with the bigger range in  $\rho_{th}$ .

## VI. FLUCTUATIONS

To show the fraction of liquid and gas phase and the transition to uniform matter, we plotted the threshold density profiles for various calculations in FIG. 4. For the lowest temperature and low mean density, there is a big peak at small densities and a long tail to high densities. With increasing mean density a peak at high density develops. At the densities where rod(3) and slab shapes appear ( $5 \cdot 10^{-2} \text{ fm}^{-3} < \rho < 7 \cdot 10^{-2} \text{ fm}^{-3}$ ) the peaks for low and high densities have nearly the same width and height. At higher mean densities the peak for low densities disappears and only a tail remains.

With increasing temperature the double peak structure vanishes and finally a single peak around the mean

density is forming which moves successively to central density with ever higher  $T$ . Consider, e.g., the case of the mean density of  $6.4 \cdot 10^{-2} \text{ fm}^{-3}$  in FIG. 4: We can observe a double peak structure for the lowest temperature  $T = 7 \text{ MeV}$ . For  $T = 11.2 \text{ MeV}$  we can separate the two phases at a mid value of the peak and still observe pasta structure. For higher temperatures no pasta structure can be observed. Only fluctuations around the mean value plotted as a dashed line remain, so that it is considered as uniform matter.

As the pasta structures vanish with higher density, the variance from the mean value of the calculation of these plots decreases. Going through the systematics of the results, we found as a reasonable value for a limit of the variance to observe pasta structures  $10^{-4} \text{ fm}^{-6}$ . The phase separation line computed with this observable is displayed in FIG. 2 as a bold line.

## VII. CONCLUSION

In this work we have studied the nuclear composition of supernova matter, i.e. matter at sub-nuclear densities. To this end, we used self-consistent nuclear mean-field theory at the level of time-dependent Hartree-Fock (TDHF) using the Skyrme energy functional. We solve the TDHF equations without any symmetry restrictions on a fully three dimensional coordinate-space grid using periodic boundary conditions to simulate infinite matter. The initial state is prepared by placing  $N_\alpha$   $\alpha$  particles stochastically over the simulation box and adding  $2N_\alpha$  neutrons in plane waves which amounts to a 2:1 mix of neutrons to protons. Scanning cases with different  $N_\alpha$  allows to tune different average densities. These initial states carry already a minimum of excitation energy because of the interaction energy of the  $\alpha$  particles and the neutrons. We have additionally varied the excitation state by initializing the  $\alpha$  particles and the neutrons with a certain amount of kinetic energy. As a measure for the actual excitation, we introduce a rough estimate for the resulting temperature based on the excitation energy (relative to the true ground state of the given case). The thus given initial states evolve to a topologically stable state of pasta matter within about 1000 fm/c. This allows us to deduce a map of pasta shapes in the plane of temperature and density. Those TDHF results agree qualitatively with the phase diagram calculated in QMD [36]. In realm of “rod” structure, we include further sub-structures, coined rod(2) and rod(3), which appeared in earlier Hartree-Fock calculations [15, 21].

As a further means for characterizing these rather involved three-dimensional structures, we use Minkowski functionals which have been proven to be useful measures for structures of fuzzy material. As we deal with smooth density distributions which cover continuously all values between zero and maximum density, we produce 0 to 1 step functions by setting a threshold density and we consider the Minkowski functionals as function

of this threshold density. This method of analysis allows to characterize the various shapes in terms of a few key numbers. This allows, e.g., to discriminate reliably the different rod structures, or to work out the smooth transition to uniform matter at high temperature. By taking the variance of the density profile as a complementing further observable, we can define a phase border between uniform matter and pasta shapes.

## ACKNOWLEDGMENTS

This work was supported by the Bundesministerium für Bildung und Forschung (BMBF) under contract numbers 06ER9063 and 06FY9086, the German science foundation (DFG) for the grant ME1361/11 as part of the research unit 'Geometry and Physics of Spatial Random Systems' and by Grants-in-Aid for Scientific Research on Innovative Areas through No. 24105008 provided by MEXT. The calculations for this work have been performed on the computer cluster of the Center for Scientific Computing of J. W. Goethe-Universität Frankfurt. B.S., K.I., and J.A.M. acknowledge the hospitality of the Yukawa Institute for Theoretical Physics, where this work was initiated.

- 
- [1] H. A. Bethe, *Rev. Mod. Phys.* **62**, 801 (1990).
- [2] H. Suzuki, *Physics and Astrophysics of Neutrinos*, edited by M. Fukugita and A. Suzuki (Springer, Tokyo, 1994).
- [3] A. Burrows, ArXiv e-prints (2012), arXiv:1210.4921.
- [4] D. Q. Lamb *et al.*, *Phys. Rev. Lett.* **41**, 1623 (1978).
- [5] R. Ogasawara and K. Sato, *Prog. Theor. Phys.* **68**, 222 (1982).
- [6] P. Bonche and D. Vautherin, *Nucl. Phys. A* **372**, 496 (1981).
- [7] C. J. Pethick and D. G. Ravenhall, *Ann. Rev. Nucl. Part. Sci.* **45**, 429 (1995).
- [8] N. Chamel and P. Haensel, *Living Rev. Relativ.* **11** (2008).
- [9] D. G. Ravenhall, C. J. Pethick, and J. R. Wilson, *Phys. Rev. Lett.* **50**, 2066 (1983).
- [10] M. Hashimoto, H. Seki, and M. Yamada, *Prog. Theor. Phys.* **71**, 320 (1984).
- [11] C. Pethick and A. Potekhin, *Phys. Lett. B* **427**, 7 (1998).
- [12] G. Watanabe, K. Iida, and K. Sato, *Nucl. Phys. A* **687**, 512 (2001), erratum *ibid.* 726, 357 (2003).
- [13] R. Williams and S. Koonin, *Nucl. Phys.* **435**, 844 (1985).
- [14] M. Lassaut *et al.*, *Astron. Astrophys.* **183**, L3 (1987).
- [15] W. G. Newton and J. R. Stone, *Phys. Rev. C* **79**, 055801 (2009).
- [16] T. Maruyama *et al.*, *Phys. Rev. C* **57**, 655 (1998).
- [17] H. Sonoda *et al.*, *Phys. Rev. C* **77**, 035806 (2008).
- [18] C. J. Horowitz, M. A. Pérez-García, and J. Piekarewicz, *Phys. Rev. C* **69**, 045804 (2004).
- [19] C. J. Horowitz *et al.*, *Phys. Rev. C* **70**, 065806 (2004).
- [20] H. Sonoda *et al.*, *Phys. Rev. C* **75**, 042801 (2007).
- [21] F. Sébille, S. Figerou, and V. de la Mota, *Nucl. Phys. A* **822**, 51 (2009).
- [22] F. Sébille, V. de la Mota, and S. Figerou, *Phys. Rev. C* **84**, 055801 (2011).
- [23] L. A. Santaló, *Integral Geometry and Geometric Probability* (Addison-Wesley, 1976).
- [24] R. Schneider and W. Weil, *Stochastic and Integral Geometry (Probability and Its Applications)* (Springer, 2008).
- [25] K. Mecke, *Int. J. Mod. Phys. B* **12**, 861 (1998).
- [26] K. Mecke and D. Stoyan, *Statistical Physics and Spatial Statistics - The Art of Analyzing and Modeling Spatial Structures and Pattern Formation*, 1st ed., Lecture Notes in Physics, Vol. 554 (Springer, 2000).
- [27] G. E. Schröder-Turk *et al.*, *Adv. Mater.* **23**, 2535 (2011).
- [28] W. E. Lorensen and H. E. Cline, *SIGGRAPH Comput. Graph.* **21**, 163 (1987).
- [29] K. Mecke, *Phys. Rev. E* **53**, 4794 (1996).
- [30] K. Mecke, T. Buchert, and H. Wagner, *Astron. Astrophys.* **288**, 697 (1994).
- [31] M. Kerscher *et al.*, *Astron. Astrophys.* **373**, 1 (2001).
- [32] M. Kerscher, K. Mecke, and P. Schücker, *Astron. Astrophys.* **377**, 1 (2001).
- [33] J. Schmalzing *et al.*, *Astrophys. J.* **526**, 568 (1999).
- [34] G. Watanabe *et al.*, *Phys. Rev. C* **68**, 035806 (2003).
- [35] G. Watanabe *et al.*, *Phys. Rev. C* **69**, 055805 (2004).
- [36] H. Sonoda *et al.*, *Phys. Rev. C* **77**, 035806 (2008).
- [37] P. A. M. Dirac, *Math. Proc. Cambridge* **26**, 376 (1930).
- [38] M. Bender, P.-H. Heenen, and P.-G. Reinhard, *Rev. Mod. Phys.* **75**, 121 (2003).
- [39] E. K. U. Gross, J. F. Dobson, and M. Petersilka, *Top. Curr. Chem.* **181**, 81 (1996).
- [40] J. W. Negele, *Rev. Mod. Phys.* **54**, 913 (1982).
- [41] K. T. R. Davies *et al.*, in *Treatise on Heavy-Ion Physics, Vol. 3 Compound System Phenomena*, edited by D. A. Bromley (Plenum Press, New York, 1985) p. 3.
- [42] C. Simenel and P. Chomaz, *Phys. Rev. C* **68**, 024302 (2003).
- [43] J. Maruhn *et al.*, *Phys. Rev. C* **71**, 064328 (2005).
- [44] A. S. Umar and V. E. Oberacker, *Phys. Rev. C* **73**, 054607 (2006).
- [45] A. S. Umar and V. E. Oberacker, *Phys. Rev. C* **74**, 021601 (2006).
- [46] E. Chabanat *et al.*, *Nucl. Phys. A* **635**, 231 (1998).
- [47] N. W. Ashcroft and N. D. Mermin, *Solid State Physics* (Brooks Cole, 1976).
- [48] H. Pais and J. R. Stone, *Phys. Rev. Lett.* **109**, 151101 (2012).
- [49] H. Hadwiger, *Vorlesungen über Inhalt, Oberfläche und Isoperimetrie* (Springer, 1957).
- [50] G. E. Schröder-Turk *et al.*, ArXiv e-prints (2010), arXiv:1009.2340.
- [51] Implementations can be found at [www.theorie1.physik.fau.de](http://www.theorie1.physik.fau.de).

- [52] W. Mickel *et al.*, *Biophys. J.* **95**, 6072 (2008).
- [53] S. T. Hyde, *Z. Kristallogr.* **187**, 165 (1989).